

Holographic formation of optical-vortex filaments

Z. S. Sacks, D. Rozas, and G. A. Swartzlander, Jr.

Department of Physics, Worcester Polytechnic Institute, Worcester, Massachusetts 01609-2280

Received December 18, 1997; revised manuscript received April 29, 1998

An optical-vortex filament is characterized by a dark core of vanishing size and fluidlike propagation dynamics in the near-field region. This type of phase singularity does not naturally occur as an eigenmode of a cylindrically symmetric system, but it can be easily formed by computer-generated holography. The size of the core is an important attribute affecting vortex-vortex interactions within a laser beam. Here we demonstrate a means to minimize the core size, and we experimentally show that a beam-to-core size ratio exceeding 175 may be readily achieved. © 1998 Optical Society of America [S0740-3224(98)01708-1]

OCIS code: 090.1760.

1. INTRODUCTION

Optical vortices (OV's) are fascinating owing to their robust topological structure, their ubiquitous presence in many scattering systems,¹⁻³ and their similarity to vortices in other physical systems. These so-called field defects have recently attracted considerable attention in nonlinear optics,⁴ owing to both their spontaneous formation in laser cavities^{5,6} and to their appearance as solitons in self-defocusing media.⁷⁻⁹ Most recently, OV's have been found to exhibit fluidlike propagation dynamics in both linear and nonlinear media.¹⁰⁻¹³ What is more, the control over initial conditions in optics enables one to investigate experimentally the effective interaction between vortices using techniques that are not available in other physical systems such as superfluids and other Bose condensates. For example, the number, position, and topological charge of vortices may be precisely controlled, and optical measurements may, in many cases, be made with minimal perturbations to the system.

As in fluids, various types of vortices may occur in optics. Here we explore those having a core size much smaller than other feature sizes (but much larger than the wavelength). In this case the core may initially be considered as a filament. In self-defocusing media the filament propagates intact as a soliton,⁷ whereas in linear media, the filament diffracts and radiates ring structures. Compared with a conventional large-core vortex, the angular-momentum density¹⁴ of a vortex filament will be distributed closer to the vortex center. The propagation dynamics of OV's strongly depends on their phase and amplitude structure. Although the phase profiles of the large-core OV and the vortex filament may be identical, the difference in amplitude functions gives rise to two distinct propagation regimes.^{12,13} Namely, neighboring large-core OV's do not affect each other's motion, while vortex filaments exhibit fluidlike dynamics in the near-field region. To investigate experimentally the propagation dynamics of vortex filaments, holographic or diffractive masks that exhibit good optical quality are required. Nanolithography may be used to create diffractive optical elements having submicrometer features; however, such masks are formidably expensive and are not readily avail-

able. Contact lithography may also be used, but this approach is labor intensive because many well-aligned master masks are needed to achieve adequate phase resolution. A more convenient method of constructing vortex masks uses computer-generated holography^{15,16} (CGH), which has the advantages of rapid and inexpensive production, simple fabrication steps, and adequate phase control.

The objective of this investigation is to achieve vortex-filament sizes at least two orders of magnitude smaller than the overall beam size (for comparison, the ratio of the beam size to the vortex-core size for a conventional doughnut mode of a laser is only ~ 3). As described in Section 6, we succeeded in obtaining a ratio of ~ 175 . This report is organized as follows. A description of the free space propagation of an OV is presented in Section 2 for both a point vortex and a conventional vortex on a Gaussian background beam. The field in the focal plane of a lens (or far-field regime) is determined in Section 3 for a point vortex on a Gaussian and pillbox background beam. In Section 4 we discuss the holographic representation of a point vortex on a digitized black-and-white holographic medium. We explain in Section 5 how spatial filtering affects the vortex-core size. The vortex created with the CGH may be used to create a high-efficiency hologram in a photopolymer, as discussed in Section 6. Finally we present our measurements of the vortex core in Section 7, and we summarize our results in Section 8.

2. PROPAGATION OF AN OPTICAL VORTEX

An optical vortex, or field defect, is a point singularity in the transverse phase of an optical field. A monochromatic beam propagating in the z direction and containing a single vortex transversely centered at the origin ($\rho = 0$) may be expressed by the scalar envelope function:

$$u(\rho, \phi, z) = A_m(\rho, z) \exp(-im\phi) \exp[i\Phi_m(\rho, z)], \quad (1)$$

where (ρ, ϕ, z) are cylindrical coordinates with the optical axis aligned along the z axis, m is a signed integer called the topological charge, and the field is assumed to

oscillate as $\exp(ikz - i\omega t)$, where $k = 2\pi/\lambda$ is the wave number and λ is the wavelength. For convenience we shall assume $m > 0$. The amplitude, A_m , is a real function that vanishes both asymptotically and at the center of the vortex core: $A_m(\rho = 0, z) = A_m(\rho \rightarrow \infty, z) = 0$ for all z . For convenience we assume $\Phi_m(z = 0) = 0$. The initial amplitude and phase profiles are depicted in Fig. 1. The equiphase surface of the propagating electric field, $kz - m\phi + \Phi_m = \text{const.}$, defines a helix circling the z axis with a pitch of $m\lambda$.

An important attribute of the vortex is that its core remains dark as the beam propagates. This may be understood from the point of view of destructive interference between rays diffracted into the core. As described below, the vortex-core size, w_v , and the core-intensity profile significantly affect the propagation dynamics. Although strictly nonphysical, a point vortex is a conceptually useful construct whose core size is vanishingly small, at least in the initial plane, $z = 0$, such that the beam-to-core size ratio, $\beta = w_0/w_v$, approaches infinity (or at least w_0/λ).

The paraxial approximation may be used to describe the beam if $w_v \gg \lambda$, in which case the diffracting beam may be described by the Fresnel integral:¹⁷

$$u(x, y, z) = (i\lambda z)^{-1} \int_{-\infty}^{\infty} \int_{-\infty}^{\infty} dx_0 dy_0 u_0(x_0, y_0) \times \exp\{i(k/2z)[(x - x_0)^2 + (y - y_0)^2]\}, \quad (2a)$$

which may be expressed in cylindrical coordinates by making the change of variables: $x_0 = r \cos \theta$, $y_0 = r \sin \theta$, $x = \rho \cos \phi$, and $y = \rho \sin \phi$:

$$u(\rho, \phi, z) = (i\lambda z)^{-1} \exp[i(k/2z)\rho^2] \times \int_0^{\infty} \int_0^{2\pi} r dr d\theta h(r) u(r, \theta) \times \exp[-i(k/z)r\rho \cos(\theta - \phi)], \quad (2b)$$

where $h(r) = \exp[i(k/2z)r^2]$. The coordinates of the initial field are represented by (x_0, y_0) or (r, θ) , whereas in all other planes ($z \neq 0$) the coordinates are (x, y) or (ρ, ϕ) . Assuming an initial vortex field as discussed for Eq. (1), the Bessel integral¹⁸ may be substituted into Eq. (2b):

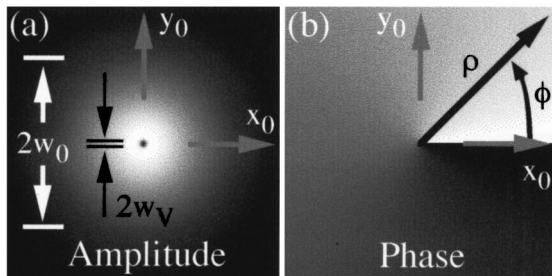


Fig. 1. Transverse profiles of a beam containing a vortex of topological charge $m = 1$. (a) Intensity profile showing a dark core of diameter, $2w_v$, on a Gaussian background field of radial size w_0 . (b) Phase profile where white and black correspond to a vortex phase of zero and -2π , respectively.

$$J_m(a) = (2\pi)^{-1} \int_0^{2\pi} d\theta \exp[-im(\theta - \pi/2)] \times \exp(-ia \cos \theta) \quad (3)$$

to obtain

$$u(\rho, \phi, z) = (2\pi/i\lambda z) \exp[-im(\phi + \pi/2)] \exp[ik\rho^2/2z] \times \int_0^{\infty} r dr h(r) A_m(r) J_m(\rho k r/z). \quad (4)$$

Setting $\xi = \rho k/z$, the integral in Eq. (4) may be expressed as a Hankel transform of order m operating on the function $f(r) = h(r)A_m(r)$ (Ref. 19):

$$H_m\{f(r)\} = \int_0^{\infty} r dr f(r) J_m(\xi r). \quad (5)$$

Case 1. Before examining the propagation characteristics of a point vortex, let us first, for comparison purposes, review a better known field, namely, the so-called doughnut modes of a cylindrical system such as a laser. Assuming a Gaussian background field, these modes may be expressed in the form of Eq. (1), with an initial amplitude function:

$$A_m(r, z = 0) = (r/L)^m \exp(-r^2/w_0^2), \quad (6)$$

where L characterizes the slope (but not the size) of the vortex, and w_0 is the initial size of the beam waist. We shall refer to this type of vortex as an r^m vortex, given that its core is characterized by the function r^m . The Hankel transform required to describe the propagation of this beam is

$$H_m\{f(r)\} = \int_0^{\infty} dr r^{m+1} \exp(-pr^2) J_m(\xi r) = [\xi^m/(2p)^{m+1}] \exp(-\xi^2/4p), \quad (7)$$

where $p = (1 - iz_0/z)/w_0^2$ and $z_0 = kw_0^2/2$. After combining terms, the propagating field may be expressed in the form of Eq. (1), where

$$A_m(\rho, z) = [w_0/w(z)] [\rho w_0/Lw(z)]^m \exp[-\rho^2/w^2(z)], \quad (8a)$$

$$\Phi_m(\rho, z) = -(m + 1) \tan^{-1}(z/z_0) + k\rho^2/2R(z), \quad (8b)$$

where $w(z) = w_0[1 + (z/z_0)^2]^{1/2}$ is the beam size and $R(z) = z[1 + (z_0/z)^2]$ is the radius of curvature of the wave front. The beam-to-core size ratio, β , may be determined by calculation of the intensity, which has a maximum, $|u_0(z)|^2 = [w_0/w(z)]^2 (m/2e)^m (w_0/L)^{2m}$, in the transverse plane at the radial position, $\rho = (m/2)^{1/2} w(z)$:

$$|u(\rho, \phi, z)/u_0(z)|^2 = (2e/m)^m [\rho/w(z)]^{2m} \times \exp[-2\rho^2/w^2(z)]. \quad (9)$$

Equation (9) indicates that the core size varies in proportion to the beam waist for all z , and thus β is a constant of motion for an r^m vortex. We have numerically determined the ratio of the half-width at half-maximum sizes from Eq. (9): β_{HWHM} equals 3.40, 2.34 and 1.99 for m equals 1, 2, and 3, respectively. These small constants

suggest it is not possible to achieve a facsimile of a point vortex with $\beta \gg 1$ for any value of charge from a cylindrical system such as a laser.

Case 2. Let us now examine the propagation of an initially ideal point vortex. The initial amplitude may be expressed as a Gaussian beam without an explicit core function, $A_m(r) = \exp(-r^2/w_0^2)$ for all m . The Hankel transform of $h(r)A_m(r)$ may be expressed in terms of complex Bessel functions:

$$H_m\{f(r)\} = \int_0^\infty r \exp(-pr^2) J_m(\xi r) dr = (\pi^{1/2} \xi / 8p^{3/2}) \times \exp(-\gamma) [I_{(m-1)/2}(\gamma) - I_{(m+1)/2}(\gamma)], \quad (10)$$

where $I_\nu(\gamma)$ is the modified Bessel function of the first kind of order ν , and ξ and p are given above, and

$$\gamma = \xi^2 / 8p = (1/2)[\rho/w(z)]^2(1 + iz_0/z), \quad (11a)$$

$$\xi / 8p^{3/2} = (w_0 z_0 / 4)(\rho/z)(1 + (z_0/z)^2)^{-3/4} \times \exp\{(3i/2)[\pi/2 - \tan^{-1}(z/z_0)]\}. \quad (11b)$$

The propagating envelope function may be written in the form of Eq. (1), with

$$A_m(\rho, z) = \frac{\sqrt{\pi}}{2} \frac{\rho}{w_0} \left(\frac{z_0}{z}\right)^{5/4} \left[\frac{z_0}{R(z)}\right]^{3/4} \exp\left[-\frac{1}{2} \frac{\rho^2}{w^2(z)}\right] \times [I_{(m-1)/2}(\gamma) - I_{(m+1)/2}(\gamma)], \quad (12a)$$

$$\Phi_m(\rho, z) = -m \frac{\pi}{2} + \frac{\pi}{4} + \left(\frac{\rho}{w_0}\right)^2 \frac{z_0}{z} \left[1 - \frac{w_0^2}{2w^2(z)}\right] - \frac{3}{2} \tan^{-1}\left(\frac{z}{z_0}\right), \quad (12b)$$

where $A_m(\rho, z)$ is the complex amplitude. The intensity profile, $|A_m(\rho, z)|^2$, plotted in Fig. 2, is characterized by high spatial frequency ringing in the near-field region,

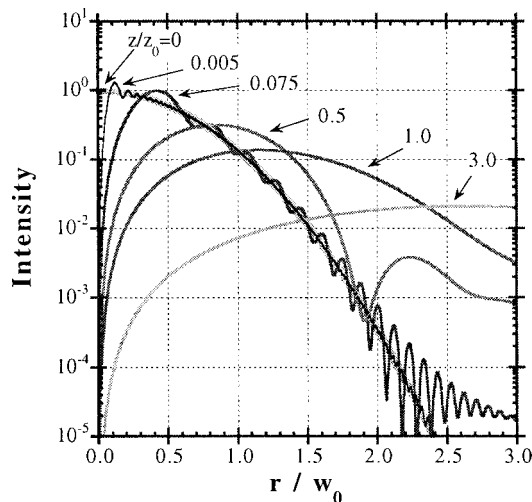


Fig. 2. Radial intensity distribution (arbitrary units) of a propagating beam initially containing an ideal point vortex on a Gaussian background field of size w_0 , showing rapid oscillations in the near-field regime and a smooth beam for $z/z_0 > 1$, where z_0 is the diffraction length.

$z/z_0 \ll 1$, and smooth profiles for $z/z_0 > 1$. As expected, the width of the vortex increases owing to diffraction, and thus β decreases as the beam propagates. In contrast to case 1, the vortex is neither an autonormal function nor an eigenmode of a cylindrical cavity, and β is not a constant of motion.

3. FOCUSED OPTICAL VORTEX

Spatial filtering, which is described in Section 5, takes advantage of the far-field profile, or, more precisely, the electric field in the focal plane of a lens. Let us examine the field in this regime for a lens of focal length, f . If the field, $u_0(r_0, \theta_0)$, is known at the front focal plane of a lens, then the field profile at back focal plane is the Fourier transform of u_0 . For a field having the form of Eq. (1), the transformed field in the focal plane [with transverse coordinates, (ρ_f, ϕ_f)] may be written:

$$u_f(\rho_f, \phi_f) = (i\lambda f)^{-1} \int_0^\infty \int_0^{2\pi} u_0(r_0, \theta_0) r_0 \times \exp[-i(kr_0\rho_f/f)\cos(\theta_0 - \phi_f)] dr_0 d\theta_0 = (k/f) \exp[-i(m+1)\pi/2] \times \exp(im\phi_f) \int_0^\infty A_m(r_0) J_m(kr_0\rho_f/f) r_0 dr_0 = \exp[-i(m+1)\pi/2] \exp(im\phi_f) A'_m(\rho_f), \quad (13)$$

where $A_m(r_0)$ and $A'_m(\rho_f)$ are amplitude functions in the front and back focal planes, respectively. Focused vortex beams are particularly useful as optical traps.²⁰ For point vortices, background fields of particular interest include both Gaussian and pillbox profiles. In the former case we obtain

$$A'_m(\rho_f) = \frac{\pi^{1/2}}{2} \left(\frac{z_0}{f}\right)^2 \frac{\rho_f}{w_0} \exp(-\gamma_f) [I_{(m-1)/2}(\gamma_f) - I_{(m+1)/2}(\gamma_f)], \quad (14)$$

where $\gamma_f = (1/2)(\rho_f/w'_0)^2$, and $w'_0 = \lambda f/\pi w_0$. For a pillbox profile of radius R , containing a vortex of charge $m = 1$, we obtain

$$A'_1(\rho_f) = -(\pi R/2\rho_f) [J_1(\rho_f/\rho'_0) \mathbf{H}_0(\rho_f/\rho'_0) - J_0(\rho_f/\rho'_0) \mathbf{H}_1(\rho_f/\rho'_0)], \quad (15)$$

where $\rho'_0 = f/kR$, and J_n and \mathbf{H}_n are Bessel and Struve functions of order n , respectively. The field profiles for the Gaussian and pillbox cases are shown in Fig. 3 for $m = 1$ [for comparison the vortexless cases ($m = 0$) are also shown]. The profiles have all been normalized by the same intensity gain factor, w_0/w'_0 , where we assume $R = w_0$.

The solutions of Eqs. (14) and (15), represented in Fig. 3, exhibit several obvious features. As expected, the field vanishes at the origin owing to destructive interference within the vortex core. Unlike a planar wave front having a hole that tends to fill owing to diffraction, the vortex core remains dark. This result illustrates the principle of conservation of topological charge. The wall of the vortex core reaches a peak closer to the core for the Gaussian

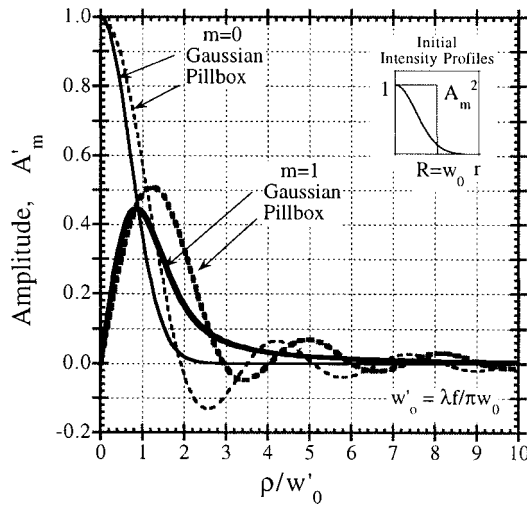


Fig. 3. Numerical integration of Eq. (13), showing the radial intensity distributions in the focal plane for an initial point vortex ($m = 1$) on Gaussian and pillbox beams, with characteristic sizes w_0 and $R = w_0$, respectively. For comparison the nonvortex beams ($m = 0$) are also shown. The radial coordinate is scaled by the diffraction-limited spot size, $w'_0 = \lambda f / \pi w_0$, and the amplitude is scaled by the optical gain factor, w_0 / w'_0 .

case, compared with the pillbox case. Furthermore, the outer perimeter of the beam also decays faster for the Gaussian background, decreasing as ρ_f^{-2} for large ρ_f / w'_0 . For the pillbox case the peaks of the oscillating tail fall as ρ_f^{-1} . We note that even though the near-field beams exhibit diffractive ringing in the vicinity of the core, as shown in Fig. 2, the far-field profile is smooth for a Gaussian background. Finally, we see that the intensity vanishes at $\rho_f / w'_0 \approx 2.9$ (i.e., at $\rho_f \approx 0.9 \times \lambda f / R$) for the pillbox case and diminishes to 2% of its peak for the Gaussian case.

4. COMPUTER-GENERATED HOLOGRAPHY

To construct a CGH of a vortex, we follow the approach of Bazhenov *et al.*,¹⁵ and we numerically compute the interferogram of two waves: a planar reference wave and an object wave containing the desired holographic image. Here we choose the object wave to be a point vortex of unit charge on an infinite background field of amplitude C_1 ,

$$E_{\text{obj}} = C_1 \exp(-i\theta), \quad (16a)$$

and a reference wave of amplitude C_0 , whose wave vector subtends the optical axis at the angle ψ_1 ,

$$E_{\text{ref}} = C_0 \exp(i2\pi x / \Lambda), \quad (16b)$$

where $\Lambda = \lambda / \sin \psi_1$ is the spatial period of the plane wave in the transverse plane. To achieve unity contrast, we let $C_1 = C_0$. The resulting interferogram, depicted in Fig. 4(a), is characterized by nearly parallel grating lines, except for a forking pattern in the vicinity of the core, and may be expressed as

$$\begin{aligned} I_{z=0}(x, \theta) &= |E_{\text{obj}} + E_{\text{ref}}|_{z=0}^2 \\ &= 2C_0^2 [1 + \cos(2\pi x / \Lambda + \theta)]. \end{aligned} \quad (17)$$

Note that Eq. (17) may be viewed as the power spectrum of the series

$$f(x, \theta) = \sum_{m=-\infty}^{\infty} C_m \exp(im\theta) \exp(i2\pi m x / \Lambda) \quad (18)$$

with $C_0 = C_1$ being the only nonzero coefficients. In general, any interferogram represented by the function $|f(x, \theta)|^2$ will have a vortex of charge m , diffracted into each of the m th-order beams whose diffraction angle is given by the grating formula:

$$\psi_m = \arcsin(m\lambda / \Lambda) \equiv \arcsin(m\lambda N_p / \eta), \quad (19)$$

where N_p is the resolution of the laser printer or other holographic medium, and

$$\eta = \Lambda N_p \quad (20)$$

is the unitless period of the CGH, as measured in units of resolvable dots.

Once Eq. (17) is numerically calculated and represented as a gray-scale image on a computer, it may be either photographed or transferred to acetate film by a laser printer. The latter approach is favorable because commercial laser printers allow large format sizes without the need for high-quality laboratory lens systems. Like in a photographic film, however, true gray-scale images are not possible; rather, the finest features appear as either black or white spots. Hence the laser-printed interferogram appears as a thresholded version of Eq. (17), as shown in Fig. 4(b). High-quality laser printers have a typical resolution of $N_p = 5080$ dots per inch (dpi), which is small compared to holographic photographic film with $N_p > 1 \mu\text{m}^{-1}$. In either case the holographic image will suffer distortions from limited gray-scale and spatial resolution.

Let us first address the effects of a one-bit gray scale. A thresholding operation applied to Eq. (17) will result in a function in the form of Eq. (18). When the printed CGH is illuminated at normal incidence, a holographic image and its complex conjugate may be found at the angles, $\pm\Psi_1$, subtending the z axis in the xz plane. In addition, multiple diffraction orders will also emerge, as discussed above. The desired image may be separated

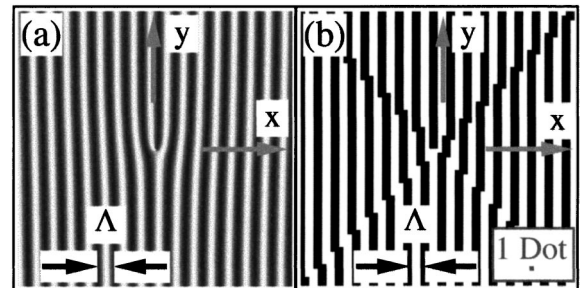


Fig. 4. (a) Interferogram of a single point vortex of charge $m = 1$. The vortex core is located at the fork of the equiphase lines. Far from the core, the lines are separated by the grating period, Λ . (b) One-bit gray-scale rendering of (a), showing grating lines of width $\Lambda/2$. The interference fringes are composed of line segments, resulting in $\eta = \Lambda N_p$ ($\eta = 4$ in this example) distinct phase domains whose boundaries radiate from the core, where N_p is the resolution of the laser printer (typically measured in dots per inch).

from the many other diffraction orders by spatially filtering the transmitted light. That is, a large collection lens may be used to focus the orders into multiple spots in the focal plane, where an aperture is then used to selectively transmit only the desired order. Spatial filtering is discussed in greater detail in Section 5.

Next we address the spatial-resolution problem. Sampling theory dictates that $\Lambda > 2/N_p$, and experience suggests $\Lambda > 8/N_p$ for the printer used in our investigations, a Linotronix Hercules printer with $N_p^{-1} = 5 \mu\text{m}$. An examination of the printed lines and dots revealed $5\text{-}\mu\text{m}$ dots with a placement accuracy of one dot, as well as a minimum consistent line width of $20 \mu\text{m}$ ($10\text{-}\mu\text{m}$ lines were randomly broken). We also found that lines drawn in the direction of the laser scan were straight, while perpendicular lines were wavy. This latter observation indicates that interferograms having nearly parallel lines, such as sparse vortex distributions, are well suited for laser-printed holograms.

Small spatial periods are favorable for achieving a small vortex-core size. That is, large values of β require small values of Λ or η . This may be understood by considering that the resolving power of a grating is equal to the number of illuminated lines. If the vortex core is the smallest resolvable feature, as desired, then, in the diffraction limit, we may assume $2w_V \approx \Lambda$, and thus

$$\beta = w_0/w_V \approx 2w_0N_p/\eta \gg 1, \quad (21)$$

where $2w_0$ is assumed to be the effective diameter of the hologram. Although this ratio can be increased by simply increasing the effective size of the hologram, in practice this approach is limited by the size and quality of the lenses in the optical system. For example, our setup uses 3.15-in (8-cm) diameter achromatic lenses.

On the other hand, large values of Λ or η , as used in Refs. 15 and 16, are required to achieve satisfactory phase resolution in the reconstructed electric field. This may be understood by considering that neighboring grating lines represent a 2π phase difference. Digitization of the space between these lines results in a digitized phase, with as many as η distinct phases over 2π rad (recall that η is also the number of printer dots per grating period). The phase resolution is therefore $N_\phi = \eta/2\pi$. Small values of η will yield a hologram whose ideally curved interference fringes appear instead as abruptly displaced line segments, as can be easily seen in Fig. 4(b) for the case $\eta = 4$. A vortex is essentially a phase object, and limiting the phase resolution will significantly affect the image quality. An appropriate value of η can be obtained from Eq. (21) once N_p and w_0 are known from experimental constraints, and a desired value β has been selected. For example, if $N_p^{-1} = 5 \mu\text{m}$, $w_0 = 25 \text{ mm}$, and $\beta = 200$, then $\eta = 50$. This will produce a core size of roughly $w_V \approx \Lambda/2 = \eta/2N_p = 125 \mu\text{m}$ on a 50-mm-diameter beam. We point out that one may be able to optically reduce the holographic image to decrease the vortex size without significantly changing β .

Whereas spatial digitization and intensity thresholding are unavoidable artifacts that constrain the rendering of a laser-printed hologram, various techniques may be employed to draw the one-bit representation of the interferogram. To control this rendering, the CGH must be writ-

ten as a command sequence that the printer can accurately interpret. For many laser printers, the command language is PostScript (PostScript is a trademark of the Adobe Corporation). The CGH PostScript-encoded data files are frequently 10–100 times larger than its binary image file, although significant compression may be achieved by coding frequently used instruction sequences into a single instruction that can be defined in a PostScript dictionary in the file header. Further reduction may be achieved by drawing lines, rather than a sequence of dots, since the former has a smaller instruction set.

Various algorithms may be used to convert the interferogram to a series of black-and-white line segments. A *thresholding* algorithm was written to calculate the intensity at every point in a grid and assign either a 0 or 1, depending on the value of a thresholding parameter (typically at half the peak intensity so that the black-and-white fringes have equal width). For a 1-in² (6.45-cm²) grid this corresponds to 5080^2 data points, and is therefore computationally intensive. Instead, a *line-walking* algorithm was designed to sweep in the x direction along the edge of the grid, looking for a relative maximum; once found, it draws a single line of width $\Lambda/2 = \eta/(2N_p)$ in mostly the y direction along the relative maximum until reaching the other edge of the grid. This method allows a significant reduction in both the computational time and the size of the image file, although it may not be used in the vicinity of the vortex, since the interference fringes fork there. The speed of this algorithm can be improved by use of a binary-search method to find the end of a straight line segment, rather than following the relative maximum point by point along a line. Since the *line-walking* algorithm cannot properly draw the line-splitting associated with the vortex, a *hybrid* algorithm was used: *thresholding* in the vicinity of the vortex and *line walking* everywhere else.

5. SPATIAL FILTERING

The effects of a finite spatial and gray-scale resolution in the CGH often require one to use spatial-filtering techniques to (1) smooth out some distortion and (2) select the desired diffraction order. Let us first examine the effects of phase distortion. The integer number (η) of distinct phases in the CGH will form phase domains, as discussed above, whose boundaries appear to radiate from the vortex core [see Fig. 4(b)]. In the near-field region, destructive interference along each domain boundary reduces the intensity by a factor of roughly $\cos^2(\pi/\eta)$. This has the effect of diffracting light into a star-burst pattern in the far-field region, shown in Fig. 5(a), with each arm bisecting a phase domain. A circular aperture placed in the focal plane of a lens, as illustrated in Fig. 5(a), may be used to eliminate the strongly diffracted components of this pattern. The filtered beam may then be reimaged and recollimated with a second lens, as depicted in Fig. 6. Numerical results, demonstrating the effect of filtering, are shown in Figs. 5(b) and 5(c). A large diameter aperture allows the transmission of high spatial frequencies, and thus a small vortex core is produced, although the beam exhibits faint stripes radiating from the core, as shown in Fig. 5(b). On the other hand, the stripes disappear when

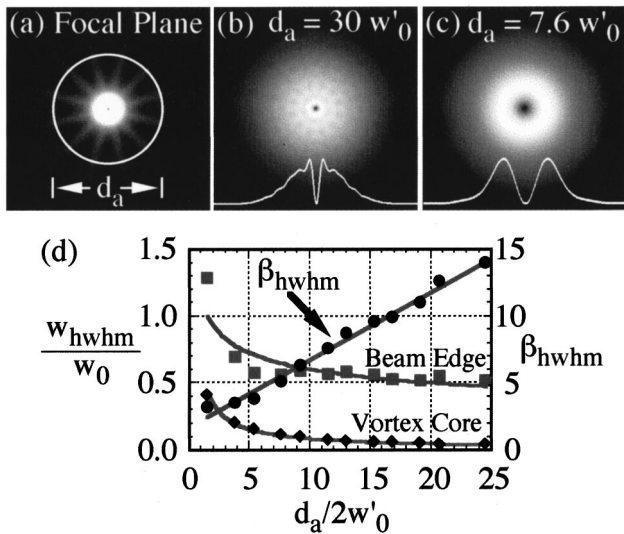


Fig. 5. (a) Finite phase resolution in the CGH produces η arms radiating from the vortex core in the focal plane of a lens. An aperture of diameter d_a may be used to spatially filter the holographic image. (b) Large apertures produce smaller cores and more distorted background fields compared with small apertures (c). The effect of aperture size on the beam-to-core size ratio, β_{HWHM} , is plotted in (d).

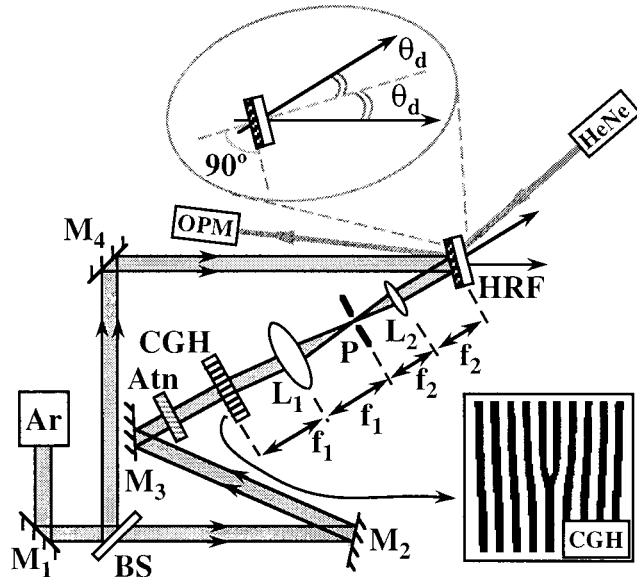


Fig. 6. Schematic of the optical system for converting the CGH into a thick phase hologram. A beam from a Spectra-Physics frequency-stabilized argon-ion laser (Ar) is directed through a glass wedge beam splitter (BS). The object beam is transmitted through the computer-generated hologram (CGH), and the first-order diffracted beam is allowed through a pinhole (P) in a spatial filter assembly. The object and reference beams are balanced with the aid of an attenuator (Atn) and made to interfere at equal angles, θ_d , with respect to the normal of the holographic recording film attached to a glass window (HRF). A helium-neon laser (HeNe) and an optical power meter (OPM) are used to monitor the efficiency of the hologram in real time.

a small aperture is used [see Fig. 5(c)]; however, both the vortex core and the beam size are now larger than in Fig. 5(b). Numerically determined measurements, plotted in Fig. 5(d), indicate that the vortex-core size is inversely proportional to the aperture size. This result is expected,

owing to the convolution of the vortex beam with the Fourier transform of the aperture function (the latter being an Airy disk). For example, an ideal point vortex would have a diffraction limited size of order $w_{\text{lim}} = 1.22 \lambda f/d_a$. Furthermore, we find that the numerically measured beam-to-core-size ratio, β_{HWHM} , increases linearly with the aperture diameter. The reason for this is that the high frequencies transmitted by a large aperture contribute to sharp features, namely, the vortex core, but have little effect on smooth features such as the diminishing perimeter of the beam. Not surprisingly, we see that large apertures are preferable to achieve large values of β . Fortunately, we find no fundamental upper limit to the value of β , and the only practical limit is dictated by the size of the optics and the hologram itself.

In practice, one may establish upper and lower bounds for the diameter of the spatial filter aperture, d_a , based on a vortex having infinite phase resolution. A lower limit may be set to diffraction-limited spot size in the focal plane:

$$d_{a,\text{min}} = c_b \lambda f/w_0, \quad (22)$$

where c_b is a constant that depends on the initial beam shape. For example, c_b equals $1/\pi$ for a Gaussian beam, 0.61 for a pillbox beam (of radial size, $R = w_0$), and roughly 0.9 for a beam containing a vortex (as discussed above in Section 3). Such a small pinhole will, however, significantly apodize the beam in the focal plane, and broaden the core (and the beam) in the image plane. A more preferable minimum size may be estimated by qualitatively examining Figs. 3 and 5(d). For the Gaussian case (with $m = 1$) the tail in the focal plane is considerably extended, with the intensity falling to 1% of its maximum at roughly $\rho_f/w'_0 = 3.5$, where $w'_0 = \lambda f/\pi w_0$. As a benchmark, one may desire $d_a \geq 7w'_0$. For the pillbox case the intensity has its first zeros at roughly ρ_f/w'_0 equal to 3, 4, and 6, and the intensity ringing subsides to $<1\%$ of its maximum at roughly $\rho_f/w'_0 = 5.4$. Thus, for pillbox background fields, one may wish to choose apertures having $d_a \geq 12w'_0$. The aperture should not be made too large, however, if one wishes to filter out unwanted diffraction orders. An upper limit of the aperture size may be set to the distance between neighboring diffraction orders:

$$d_{a,\text{max}} = f \tan \psi_1 \cong f \lambda/\Lambda. \quad (23)$$

Unfortunately, even this maximum aperture will affect the vortex-core size by filtering out the high spatial frequencies. This may be understood by the following argument. The diffraction-limited vortex-core size produced by the CGH is $w_V \approx \Lambda/2$. The effect of the spatial filter in the image plane is to perform a convolution of the holographic object with an Airy disk. If the radial size of the Airy disk, $1.22 \lambda f/d_a$, is much smaller than the features in the holographic object, then the image and the object will be nearly identical. To meet this condition, we desire $\Lambda/2 > 1.22 \lambda f/d_a$. However, this inequality cannot be satisfied for $d_a = d_{a,\text{max}}$. At best, the Airy disk will be 2.44 times larger than $\Lambda/2$. We note that the vortex core will not only broaden, owing to spatial filtering, but will also exhibit an overshoot, seen in Fig. 5(b), attributed to the Gibbs phenomenon.

Let us again consider a hologram having a finite phase resolution. If we select $d_a = d_{a,\max}$, then the image will contain lines of phase and amplitude distortion. If we select a smaller aperture, the beam-to-core size ratio will become smaller. One must therefore make a qualitative judgment. After experimentally observing the effects of several apertures, we found that a 35- μm diameter pinhole ($d_a \approx 18w'_0$) was most suitable for our optical system, which comprised a pillbox beam of radius $R = 25$ mm, a wavelength $\lambda = 514$ nm, and a lens of focal length $f = 310$ mm and a CGH with $\eta = 16$ and $\Lambda = 80$ μm . This pinhole diameter is within the expected range for a pillbox-type beam, as discussed above (see Fig. 3).

6. PHASE-HOLOGRAM CONVERSION

Although the CGH is relatively simple to produce, it is not suitable for experiments requiring an intense laser beam. The CGH absorbs roughly half the beam power and is therefore prone to damage. Increased efficiency and higher damage thresholds may be achieved by a phase, rather than an amplitude, hologram. Here we describe a method of recording the CGH image onto a photopolymer medium, e.g., DuPont holographic recording film, HRF-150.

After spatial filtering of the CGH image, we interfere the beam with a reference wave. The experimental arrangement is shown in Fig. 6. The reference beam was oriented to obtain a finer grating period, Λ' , than could be achieved with the CGH. The manufacturer suggests setting $\Lambda' \leq 5$ μm to ensure that monomers diffuse into the exposed regions to produce a refractive-index grating. If a thick, Bragg-type hologram can be written in the film, nearly all the light may be diffracted into the first diffraction order, which occurs at the angle, θ_d , given by the diffraction equation, $\lambda = \Lambda'(\sin \theta_d - \sin \theta_i)$, where θ_i is the angle of the incidence of both the object and reference waves with respect to the normal of the film, and $\theta_d = -\theta_i$. Thus, θ_d and Λ' are related by $\sin \theta_d = \lambda/2\Lambda'$. The angle used in our experiment was $\theta_d = 13.3^\circ$, which provided a grating period of $\Lambda' = 1.12$ μm .

The figure of merit used to judge whether the hologram is a thick Bragg-type or a thin Raman-Nath-type hologram is given by the quality factor:

$$Q = 4\pi d \theta_d / \Lambda' \approx 2\pi \lambda d / n(\Lambda')^2. \quad (24)$$

The manufacturer reports a film thickness of $d = 38$ μm and a nominal refractive index of $n \approx 1.5$. Values of $Q \gg 1$ allow high efficiencies. Using the parameters of our investigation, we calculate $Q \approx 65$, and thus a high diffraction efficiency may be expected. The efficiency of a Bragg hologram, η_B , may be estimated from the well-known result for a thick sinusoidal phase grating²¹:

$$\eta_B = \sin^2(\pi d \Delta n / \lambda \cos \theta_d), \quad (25)$$

where Δn may be as large as 9×10^{-3} in the photopolymer film.²² The efficiency may theoretically reach unity when the exposure induces an index change of $\Delta n \approx 7 \times 10^{-3}$. As the film is exposed, monomers in the film polymerize, resulting in an increased refractive index. The manufacturer suggests an exposure fluence of $F \approx 100$ mJ/cm^2 . If the intensities of the vortex and ref-

erence beams are balanced and the average intensity at the film is $I_{\text{ave}} = 5$ mW/cm^2 , then the maximum index modulation should develop in a time $T_{\text{exp}} \approx 20$ s. We found that much longer exposure times were required, T_{exp} of approximately 140–190 s, which may be attributed to the age of the holographic film we were using.

To achieve a high diffraction efficiency, it is advantageous to calibrate the exposure process by monitoring the diffracted power as a function of time while a hologram is being exposed. For this purpose, we used a weak He-Ne probe laser with a wavelength of 0.6328 μm and diffraction angle of 16.7°. Owing to the inverse relation between efficiency and wavelength in Eq. (25), the peak efficiency of the argon laser beam will occur when the He-Ne efficiency is at roughly 94%.

In the focal plane of lens L_2 we obtained a vortex of size $w_{\text{HWHM}} \approx 145$ μm ($\beta \approx 175$). However, since the size of the holographic film was smaller than the cross section of the signal and reference beams, the ratio β of the vortex recorded onto HRF was ~ 3 times smaller than 175.

7. ANALYSIS OF THE HOLOGRAPHIC IMAGE

The holographic image was analyzed by monitoring of intensity profiles of the propagating image from the surface of the hologram to a distance of roughly 1.8 m. This was accomplished by imaging of each object plane onto the array of a CCD camera (see Fig. 7), by a lens with focal length $f = 50.8$ mm. To obtain images of the vortex over the range of propagation distances, the imaging system was designed to provide a magnification of 1.7; hence the distance between the lens and the array was fixed at $d_i = 137$ mm. The vortex-core size and propagation characteristics were determined by analysis of 34 images, taken at 50-mm intervals along the optical axis of the holographic image. The radial intensity distribution function, $|A(\rho, z)|^2$ was determined by numerically averaging the intensity profile, $I(x, y)$, around the azimuth of the vortex core by the following procedure.

First we determined the location of the vortex center, $(x_c^{(i)}, y_c^{(i)})$, which presumably coincides with the first moment of the intensity profile,

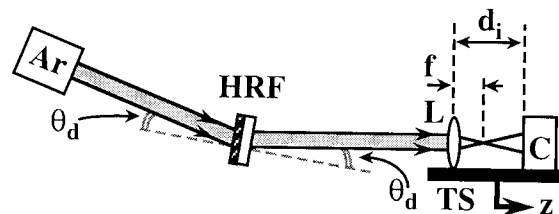


Fig. 7. Schematic of the optical system to examine the vortex recorded onto HRF. The vortex beam is imaged to a CCD array (C) by means of a lens (L) with focal length $f = 50.8$ mm and imaging distance $d_i = 137$ mm. Both C and L are mounted on a translation stage (TS), which can move along the optical axis, allowing us to monitor the transverse intensity profile at different propagation distances, z . The camera C is connected to a Macintosh IIfx computer with a frame grabber (not shown).

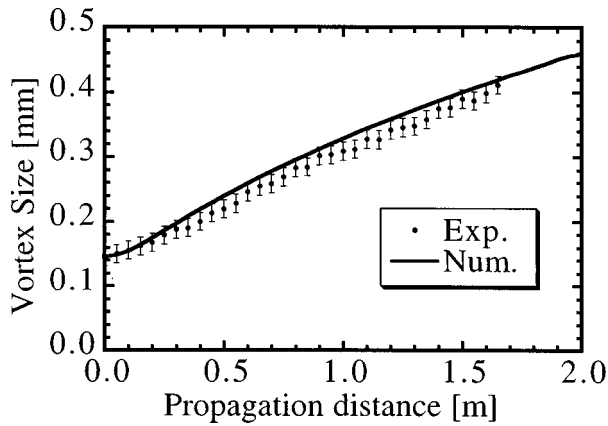


Fig. 8. HWHM size of a vortex plotted versus the propagation distance, z . The discrete points are experimental results. The curve was obtained from numerical simulations, assuming a large Gaussian beam ($w_0 = 12.8 \text{ mm} \gg w_V$) with a vortex of the amplitude profile $A(r) = \tanh(r/w_V)$, with initial $w_V = 165 \mu\text{m}$ (i.e., $w_{\text{HWHM}} = 145 \mu\text{m}$).

$$(x_c^{(i)}, y_c^{(i)}) = \frac{\iint_S (x, y) I(x, y, z^{(i)}) dx dy}{\iint_S I(x, y, z^{(i)}) dx dy},$$

where S is the area of the CCD image, and $z^{(i)}$ is the location of the object plane of the imaging system, and the integrals are performed numerically over a discrete number of grid points. Next we determined the average radial vortex-core function by numerically calculating the expression $|A(\hat{\rho}, z^{(i)})|^2 = N^{-1} \sum_{j=1}^N I(\hat{\rho}, j\Delta\phi, z^{(i)})$, where $\Delta\phi = 2\pi/N$ is the discrete angular step size between two grid points lying on a circle of radius $\hat{\rho}$ (measured in units of grid points) from the core center, and $N = \text{int}\{2\pi\hat{\rho}\}$ is the circumference of the circle in units of grid points. Finally, we obtained the HWHM values of the core size, w_{HWHM} , and compared it with the half-widths from beam-propagation simulations. The results shown in Fig. 8 are in excellent agreement over the entire scan range.

8. CONCLUSION

We have described a point vortex in the paraxial approximation, showing that it is characterized by near-field rings diffracted from the core. The high spatial frequencies of these rings transform the far-field pattern into profiles having a longer decay tail than would occur if the vortex were absent. In contrast to a doughnut mode of a laser, a point vortex is not an autormal function, and is not an eigenmode of a cylindrical guided-wave system. We discussed how pointlike vortices may be readily made by computer-generated holography, and we argued that core sizes of the order of the Nyquist limit of half the holographic grating period may be achieved. Owing to the finite gray scale and spatial resolution of the recording medium (or system), the reconstructed holographic field will be distorted, especially for small values of the grating period (as measured in the number of resolvable printed dots). Hence a trade-off exists between the core size and

the image fidelity. Spatial filtering allows one to remove unwanted diffraction orders (attributed to black-and-white holograms), as well as to smooth out phase steps (attributed to the limited phase resolution); however, filtering also broadens the core. To achieve core sizes much smaller than the characteristic beam size, i.e., pointlike vortices, one must design a system where the beam diameter, used to reconstruct the holographic image (and hence the format size of the holographic film), is much larger than the grating period of the hologram. This is not difficult to achieve in the laboratory, and thus one may easily produce pointlike optical vortices. Investigations of single and multiple vortex propagation dynamics may be conducted in both linear and nonlinear optical media. In the former case, low power beams may be used, and hence CGH's are suitable. The higher powers common to nonlinear optical experiments, however, may require one to re-record the holographic image onto a low-loss material such as a photopolymer. We have described the technique used for achieving high-efficiency holograms in DuPont HRF. Finally, we have measured the vortex-core size as the beam propagated in the near-field regime, and found a favorable comparison with theory. What is more, we found we were able to achieve a beam-to-core size ratio of 175.

ACKNOWLEDGMENTS

We are grateful to Joe Cloutier of Comp Associates, Inc. (80 Webster Street, Worcester, Massachusetts 01603), for high-resolution printing services. We also appreciate suggestions on optical design from Adriaan Walther (Department of Physics, Worcester Polytechnic Institute). This work was supported by the Research Corporation Cottrell Scholars Program and the U.S. National Science Foundation Young Investigator Program. Z. S. Sacks is now with the Center for Ultrafast Optics (University of Michigan, Ann Arbor, Michigan 48109).

REFERENCES

1. J. F. Nye and M. V. Berry, "Dislocations in wave trains," *Proc. R. Soc. London, Ser. A* **336**, 165–190 (1974).
2. M. V. Berry, *Singularities in Waves and Rays, Physics of Defects*, Les Houches Sessions XXXV, R. Balian, M. Klemann, and J.-P. Poirier, eds. (North Holland, Amsterdam, 1981), pp. 453–543.
3. N. B. Baranova, B. Ya. Zel'dovich, A. V. Mamayev, N. F. Pilipetskii, and V. V. Shkukov, "Dislocations of the wavefront of a speckle-inhomogeneous field (theory and experiment)," *Pis'ma Zh. Eks. Teor. Fiz.* **33**, 206–210 (1981) [*JETP Lett.* **33**, 195–199 (1981)].
4. M. S. El Naschie, ed., "Special issue on nonlinear optical structures, patterns, chaos," *Chaos Solitons Fractals* **4**(8/9) (1994).
5. P. Couillet, L. Gil, and F. Rocca, "Optical vortices," *Opt. Commun.* **73**, 403–408 (1989).
6. M. Brambilla, M. Cattaneo, L. A. Lugiato, R. Pirovano, F. Pratti, A. J. Kent, G.-L. Oppo, A. B. Coates, C. O. Weiss, C. Green, E. J. D'Angelo, and J. R. Tredicce, "Dynamical transverse laser patterns. I. Theory," *Phys. Rev. A* **49**, 1427–1451 (1994).
7. G. A. Swartzlander, Jr. and C. T. Law, "Optical vortex solitons observed in Kerr nonlinear media," *Phys. Rev. Lett.* **69**, 2503–2506 (1992).
8. G. S. McDonald, K. S. Syed, and W. J. Firth, "Optical vor-

- tices in beam propagation through a self-defocusing medium," *Opt. Commun.* **94**, 469–476 (1992).
9. A. W. Snyder, L. Poladian, and D. J. Mitchell, "Stable black self-guided beams of circular symmetry in a bulk Kerr medium," *Opt. Lett.* **17**, 789–791 (1992).
 10. F. S. Roux, "Dynamical behavior of optical vortices," *J. Opt. Soc. Am. B* **12**, 1215–1221 (1995).
 11. G. A. Swartzlander, Jr., Z. S. Sacks, X. Zhang, D. Rozas, and C. T. Law, "Formation and propagation of optical vortices," in *Digest of the International Quantum Electronics Conference*, 1996 OSA Technical Digest Series (Optical Society of America, Washington, D.C., 1996), p. 31.
 12. D. Rozas, C. T. Law, and G. A. Swartzlander, Jr., "Propagation dynamics of optical vortices," *J. Opt. Soc. Am. B* **14**, 3054–3065 (1997).
 13. D. Rozas, Z. S. Sacks, and G. A. Swartzlander, Jr., "Experimental observation of fluidlike motion of optical vortices," *Phys. Rev. Lett.* **79**, 3399–3402 (1997).
 14. L. Allen, M. W. Beijersbergen, R. J. C. Spreeuw, and J. P. Woerdman, "Orbital angular momentum and the transformation of Laguerre–Gaussian laser modes," *Phys. Rev. A* **45**, 8185–8189 (1992).
 15. V. Yu. Bazhenov, M. V. Vasnetsov, and M. S. Soskin, "Laser beams with screw dislocations in their wavefronts," *Pis'ma Zh. Eksp. Teor. Fiz.* **52**, 1037–1039 (1990) [*JETP Lett.* **52**, 429–431 (1990)].
 16. N. R. Heckenberg, R. McDuff, C. P. Smith, and A. G. White, "Generation of optical phase singularities by computer-generated holograms," *Opt. Lett.* **17**, 221–223 (1992).
 17. J. W. Goodman, *Introduction to Fourier Optics* (McGraw-Hill, New York, 1996), p. 67.
 18. G. A. Korn and T. M. Korn, *Mathematical Handbook for Scientists and Engineers*, 2nd ed. (McGraw-Hill, New York, 1961), p. 860.
 19. J. D. Gaskill, *Linear Systems, Fourier Transforms, and Optics* (Wiley, New York, 1978), p. 320.
 20. K. T. Gahagan and G. A. Swartzlander, Jr., "Optical vortex trapping of particles," *Opt. Lett.* **21**, 827–829 (1996).
 21. H. Kogelnik, "Coupled wave theory for thick hologram gratings," *Bell Syst. Tech. J.* **48**, 2909–2947 (1969).
 22. W. J. Gambogi, W. A. Gerstadt, S. R. Mackara, and A. M. Webber, "Holographic transmission elements using improved photopolymer films," *Proc. SPIE* **1555**, 256–266 (1991).